

<https://doi.org/10.1038/s43247-024-01322-w>

Ice acceleration and rotation in the Greenland Ice Sheet interior in recent decades

Check for updates

Anja Løkkegaard ^{1,2}✉, William Colgan ¹, Karina Hansen ^{1,2}, Kisser Thorsøe ¹, Jakob Jakobsen ¹ & Shfaqat Abbas Khan ²

In the past two decades, mass loss from the Greenland ice sheet has accelerated, partly due to the speedup of glaciers. However, uncertainty in speed derived from satellite products hampers the detection of inland changes. In-situ measurements using stake surveys or GPS have lower uncertainties. To detect inland changes, we repeated in-situ measurements of ice-sheet surface velocities at 11 historical locations first measured in 1959, located upstream of Jakobshavn Isbræ, west Greenland. Here, we show ice velocities have increased by 5–15% across all deep inland sites. Several sites show a northward deflection of 3–4.5° in their flow azimuth. The recent appearance of a network of large transverse surface crevasses, bisecting historical overland traverse routes, may indicate a fundamental shift in local ice dynamics. We suggest that creep instability—a coincident warming and softening of near-bed ice layers—may explain recent acceleration and rotation, in the absence of an appreciable change in local driving stress.

Understanding the form and flow of the Greenland Ice Sheet today is critical for simulating the future evolution of the ice sheet as climate changes. Today's ice-sheet form and flow, however, are underlain by the ice sheet's response to past climate perturbations on decadal, centennial, and even millennial time-scales. As there are very few high-quality ice velocity and elevation measurements available prior to the advent of GPS technology (Global Positioning System), there are very few constraints on multi-decadal trends in ice-sheet form and flow^{1–3}. In a review of 13 mass-balance assessments of the Greenland ice sheet, Colgan et al. highlight that virtually all recent assessments assume no ice dynamic changes within the high-elevation ice-sheet interior⁴. Additionally, studies have shown that satellite-derived velocities have challenges detecting summer acceleration above an ice elevation of 1250 in Central West Greenland, due to poor signal-to-noise ratio^{5,6}.

The Greenland ice sheet is currently in a state of decline^{7,8}. Mass is lost through processes relating either to surface mass balance or ice dynamics⁹. Warming ocean and air temperatures destabilize the ice sheet, resulting in enhanced surface melt and run-off¹⁰ and ice discharge from marine-terminating glaciers as they speed up and thin^{11,12}. These fast-flowing regions at the fringes of the ice sheet, also known as outlet glaciers, transport ice from the slow-moving interior to the ocean, providing a fast coupling between the ocean and the inland ice¹³.

As the fastest-flowing ice stream in Greenland, Jakobshavn Isbræ, or Sermeq Kujalleq, has been studied extensively. In 1997, Jakobshavn Isbræ's floating ice tongue began to disintegrate. This is believed to have been instigated by increased melt from higher ocean temperatures¹⁴. Rapid calving front retreat, acceleration, and thinning were triggered in response to this disintegration^{15–19}. By 2004, the floating tongue had almost completely disintegrated, yet acceleration and thinning continued. Many other marine-terminating outlet glaciers, such as Nioghalvfjærdsfjorden, Zachariae Isstrøm (northeast Greenland), and Helheim (southeast Greenland), are presently undergoing similar dynamic changes^{2,20}. It is, therefore, crucial to explore and discern the internal driving mechanisms sustaining this enhanced dynamic mass loss, in order to fully capture the contribution of the Greenland ice sheet to future sea-level changes^{19,21,22}.

In the 1950s and 1960s, the French Expédition Glaciologique Internationale Groenland (EGIG) undertook a number of overland ice-sheet traverses in Central West Greenland, in the vicinity of the ice-stream Jakobshavn Isbræ. These traverses included multi-year theodolite campaigns to measure ice-sheet elevation, velocity, and azimuth along inland transects. These hard-fought, and high-quality, in situ measurements now provide a singularly unique baseline against which to compare contemporary analogous measurements. During the 1990s, the NASA Program

¹Department of Glaciology and Climate, Geological Survey of Denmark and Greenland, Copenhagen, Østervoldgade 10, Copenhagen, 1350, Copenhagen K, Denmark. ²Department of Space Research and Technology, The Technical University of Denmark, Elektrovej 328, Lyngby, 2800, Kongens Lyngby, Denmark.

✉ e-mail: aloe@geus.dk

for Arctic Regional Climate Assessment (PARCA) also measured velocity and azimuth values, now using GPS, along the 2000 m elevation contour²⁵. Two of these PARCA sites overlap with our EGIG area of interest and are therefore included in this resurvey.

We reanalyze and resurvey a selection of EGIG and PARCA measurements, Fig. 1, and find non-trivial multi-decadal trends in ice-sheet flow have been occurring in recent decades. This highlights that recent perturbations in ice flow have propagated at least 100 km inland from the ice margin, well outside the main channel of fast flow. This challenges the notion of stable interior ice flow.

Results

Historical survey

The first EGIG campaign deposited and surveyed stakes along an east-west transect spanning the entirety of the Greenland ice sheet, as well as a shorter north-south transect. The stake positions were recorded in 1959 and re-measured during a subsequent campaign in 1967. Stakes along the longer east-west transect are labeled as T and a number starting with 1, whereas the numbers along the north-south transect begin at 100. An independent German expedition surveyed a subset of the stakes once more in 1991²⁴. Here, we use ice flow velocities and azimuth values calculated based on the recorded change in position for the period 1959–1967²⁵.

A reanalysis of these historical observations was performed with the goal of reproducing the reported velocity and azimuth values at each site while propagating estimated uncertainties. Also, this ensured that the

chosen calculation methods that would be used for the subsequent modern resurvey produced values directly comparable with the historical values. The reanalysis was done for 14 of the EGIG stakes located closest to the outlet of Jakobshavn Isbræ. Our inter-survey comparison requires all historical positions to be with respect to the same reference ellipsoid. However, at the time of the earliest measurements, the WGS84 reference ellipsoid had not yet been created. Consequently, the 1959–1967 locations had to be converted from the Hayford ellipsoid. A more detailed explanation of this can be found in supplementary S1. For a description of the velocity and azimuth value calculations see the method section “Historical velocity and azimuth”.

Both the recalculated velocity and azimuth values were compared with the original reported values, see Supplementary Fig. S2. The recalculated velocity and azimuth values were taken as the mean values from a Monte-Carlo simulation, see Supplementary Fig. S3. All historically reported velocity and azimuth values were successfully reproduced with the exception of T1. There were inconsistencies with the reported position of T1 in the original EGIG reports. While we have resurveyed T1, it seems reasonable to exclude its historical values from this comparison on this basis.

Modern resurvey

In 2020–2022, a subset of the original 1959 EGIG positions located closest to the outlet of Jakobshavn Isbræ was resurveyed, together with 2 of the PARCA sites, see Fig. 1. The chosen EGIG sites are T1–T5, T127a, T127–T129, and the PARCA sites are cd08 and cd38. In total 11 GPS receivers were deployed, spanning a region of ~ 1800 km². Supplementary

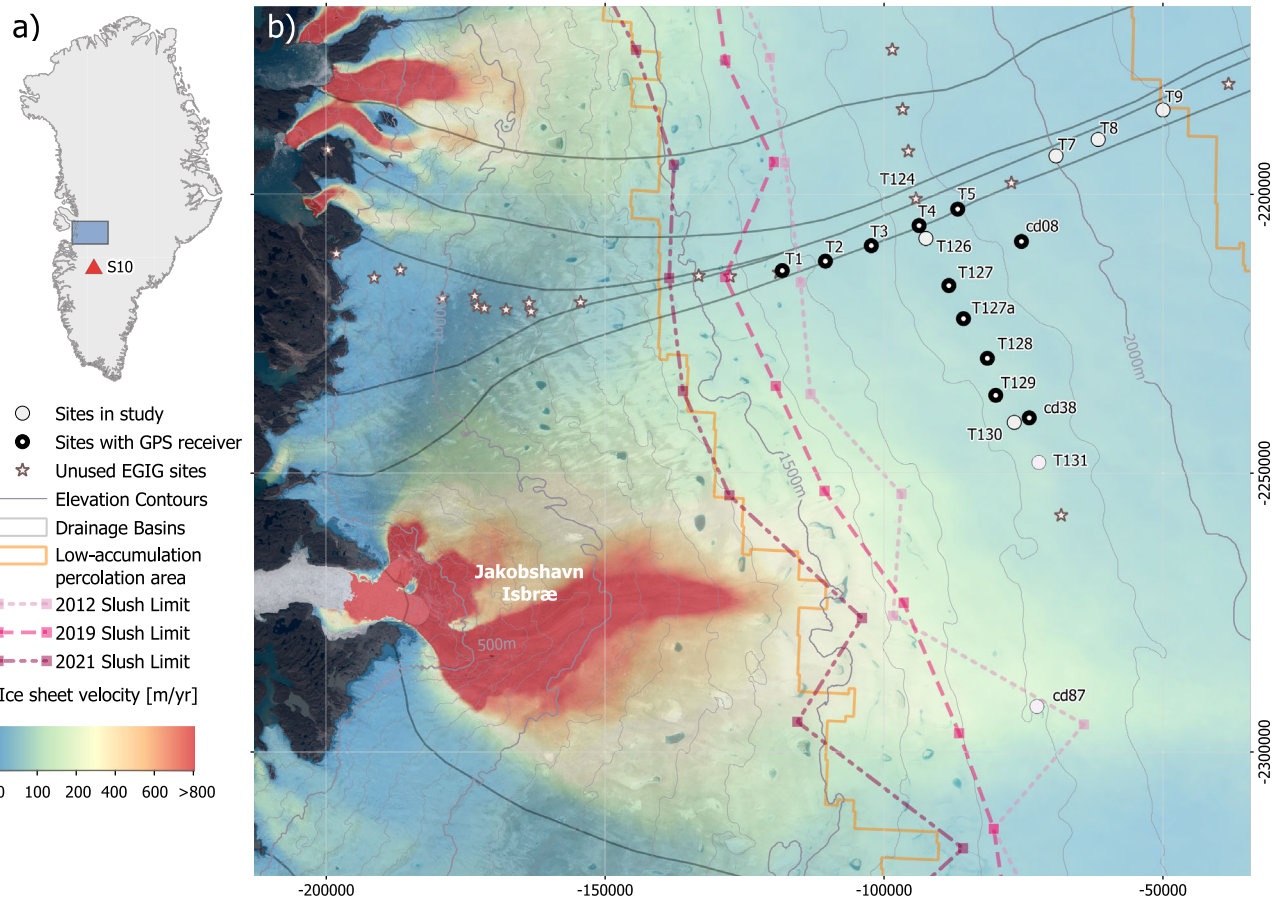


Fig. 1 | Overview of the study region. **a** The blue box indicates the general location of the study region. **b** Close-up of the study region, white circles show the location of the EGIG (prefix ‘T’) and PARCA (prefix ‘cd’) sites included in the study. Of these, black annuli plotted on top indicate sites where a GPS station was installed for this study. Stars indicate sites from the original EGIG survey not included in this study. Sites are plotted on top of surface ice flow velocities⁸⁶ and Sentinel-2 multispectral

satellite imagery, 10 m resolution from 2019⁸⁷. Also plotted are delineated drainage basins³⁶, surface elevation contours²⁶, the low accumulation percolation area⁴¹, and slush limits for the years 2012, 2019, and 2021⁴². The map is displayed in the projection coordinate system EPSG:3413 with easting and northing coordinates given in meters. This plot was created using QGreenland⁸⁸.

Table 1 | Observations overview

Site	Δt [Days]	α [°]	v [$m\ yr^{-1}$]	d [m]	dx [m]	dy [m]	Approximate period in time
T1	9.4	245.7 ± 1	142.2 ± 0.36	3.6	-3.4	-1.3	Sept. 2021
T2	80.2	247.3 ± 1	120.5 ± 0.07	26.5	-24.9	-8.9	May–Aug. 2022
T3	241.1	246.8 ± 1	120.0 ± 0.04	79.3	-74.3	-27.8	Jul–Oct. 2020 & Mar. 2021
T4	89.1	245.7 ± 1	112.5 ± 0.04	27.4	-25.5	-10.2	Jun–Sept. 2022
T5	414.9	245.9 ± 1	103.4 ± 0.06	117.6	-109.1	-43.8	Jul–Oct. 2020 & Apr–Sept. 2021
T127	382.9	244.9 ± 1	116.3 ± 0.02	121.9	-112.4	-47.2	May–Sept. 2021 & Mar–Jun. 2022
T127a	35.6	243.7 ± 1	121.9 ± 0.07	11.9	-10.9	-4.8	Jul–Aug. 2020
T128	309.8	243.3 ± 1	144.9 ± 0.03	122.9	-111.8	-51.1	Jul–Nov. 2020 & Mar–May 2021
T129	3.6	246.0 ± 1	147.0 ± 1.97	1.5	-1.4	-0.5	Oct. 2020
cd38	372.8	251.4 ± 1	132.8 ± 0.04	135.6	-129.9	-39.0	May–Sept. 2021 & Apr–Jun. 2022
cd08	292.4	243.6 ± 1	112.8 ± 0.10	90.3	-82.2	-37.4	Jun–Sept. 2021 & Mar–Apr. 2022

Derived velocity (v) and azimuth (α) values, along with estimated uncertainties. Also shown are the total observation period (Δt), the total observed horizontal movement (d) of each station, the respective components, dx and dy , and the approximate period at which observations were made.

Fig. S4 shows the station set-up. At each site, horizontal velocity and azimuth values were derived from changes in observed position over time, see section “GPS Velocity and Azimuth” under Methods and Supplementary Figs. S5–S7 Due to logistical difficulties, the observation period at each of the 11 stations ranges from a few days to > 400 days, with all stations together covering a total time span of 3 years. Of the resurveyed sites, 6 have a coverage period > 100 days, these include T3, T5, T127, T128, cd38, and cd08. The remaining 5 sites have a coverage period < 100 days, see Table 1. The logistical difficulties also mean that records are not continuous. Positions were logged at a 30 s sampling rate. Both the un-processed and processed RINEX files (see “Methods” section) are available at the GEUS dataverse <https://doi.org/10.22008/FK2/EP6P4O>.

The new points of observation are located as close as possible to the original 1959 points of observation. This, however, results in a greater distance between the new observations and the advected stake positions from the 1967–1991 survey. Comparisons over horizontal distances of > 1 ice thickness can introduce spatial gradients in the ice velocity or azimuth³. However, it is assumed that if the new and historic points lie within a distance < 1 ice thickness it is reasonable to compare the velocities. The ice thickness at each observation point was estimated from the BedMachine ice thickness map²⁶, see Fig. 2. Following this rationale, the 1967–1991 velocities

cannot be compared to the new velocities. This also shows that PARCA cd38 is not sufficiently close to EGIG site T130, which was not part of the 2020–2022 GPS survey, to reasonably make an additional EGIG/PARCA inter-comparison.

We calculated velocities and azimuths from the change in logged position, see the “Methods” section for further description. Table 1 shows the magnitude of the calculated velocity and azimuth values for the full period of observation at each of the 11 sites. The resurveyed velocities and azimuths can be seen plotted against previously observed values in Fig. 3. We observe a considerable increase in velocity across all 11 stations, ranging between 6–19 $m\ yr^{-1}$ (blue markers Supplementary Fig. S8a), corresponding to a percentage change of 5.5–14.6% (red markers Supplementary Fig. S8a). The sites furthest inland show the smallest percentage increase in velocity; 5.4% at cd08 and 8.3% at T5. The largest increase in velocity over the observation period is found at station T129 with an increase of 14.6% (closely followed by T128 and cd38). Although stations T129 and cd38 are comparable in velocity increase magnitude, the observation period of cd38 is approximately half of the T129 observation period (~30 years vs. ~60 years). This suggests that the majority of regional velocity perturbation has occurred during the post-1995 PARCA period. The observed increase in velocity mainly occurred in the easting direction, with ice flowing faster towards the west, though slight changes in the northern component were also observed, with most of the sites showing less negative southward flow (Supplementary Table S1).

We observed consistent increases in azimuth, ranging between 3–4.5°, at all 8 resurveyed EGIG sites, see Fig. 3b and Supplementary Fig. S8b). This increase is well beyond the limit of uncertainty. No statistically significant change in azimuth values was observed at the two PARCA survey sites cd08 and cd38. The change was within the uncertainty range between the two periods of observation, with azimuth values decreasing by less than 0.5°. Therefore, no conclusions are drawn about long-term azimuth shifts at cd38 and cd08.

Ice thinning

We used altimetry data to assess changes in ice geometry, as a proxy for changes in driving stress. This data originated from a number of campaigns, covering overlapping portions of the 1995–2020 period. This data was compiled and processed into an annual rate of change of surface elevation by two studies, for the period 1995–2011, and for the period 2011–2020^{27,28}. The cumulative change in surface elevation in meters of ice equivalent over the available period (1995–2020) was calculated across the Greenland Ice Sheet. Figure 4a shows marginal thinning and slight thickening in the central region. The cumulative change in surface elevation from 1995 to selected points in time, is shown along a flow-line cutting through the observation sites of the east-west transect, and plotted against surface elevation using a

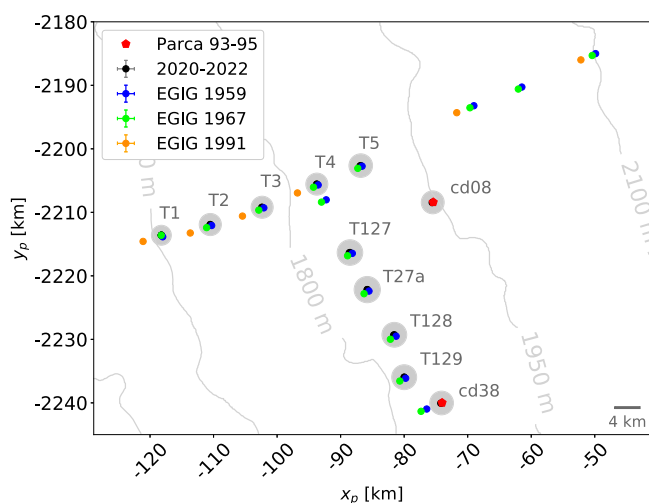


Fig. 2 | Overview of modern and historically observed positions. Gray circles have a radius of the ice thickness at each specific point²⁶. Black points show the resurveyed positions. Blue, green, and orange points show the recorded positions from the EGIG campaigns^{24,25}. The red points show positions from the PARCA campaign²³. Position uncertainties are plotted but they are too small to clearly appear on the figure.

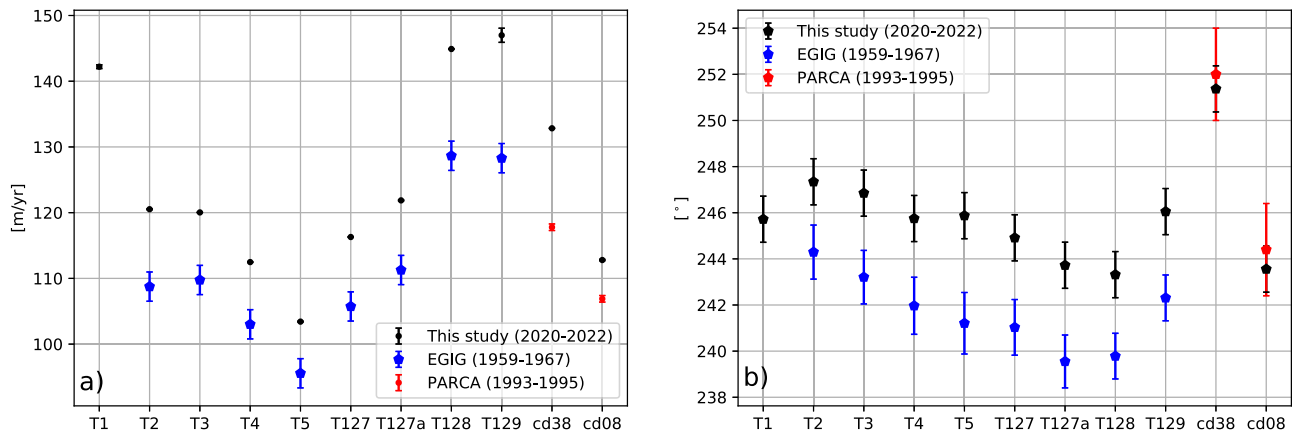


Fig. 3 | Comparison of modern resurveyed findings with historically reported values. Velocity (a) and azimuth (b) at each site for each period of observation; 1959–1967 (EGIG), 1993–1995 (PARCA), 2020–2022 (this study). Vertical bars denote associated uncertainties calculated here.

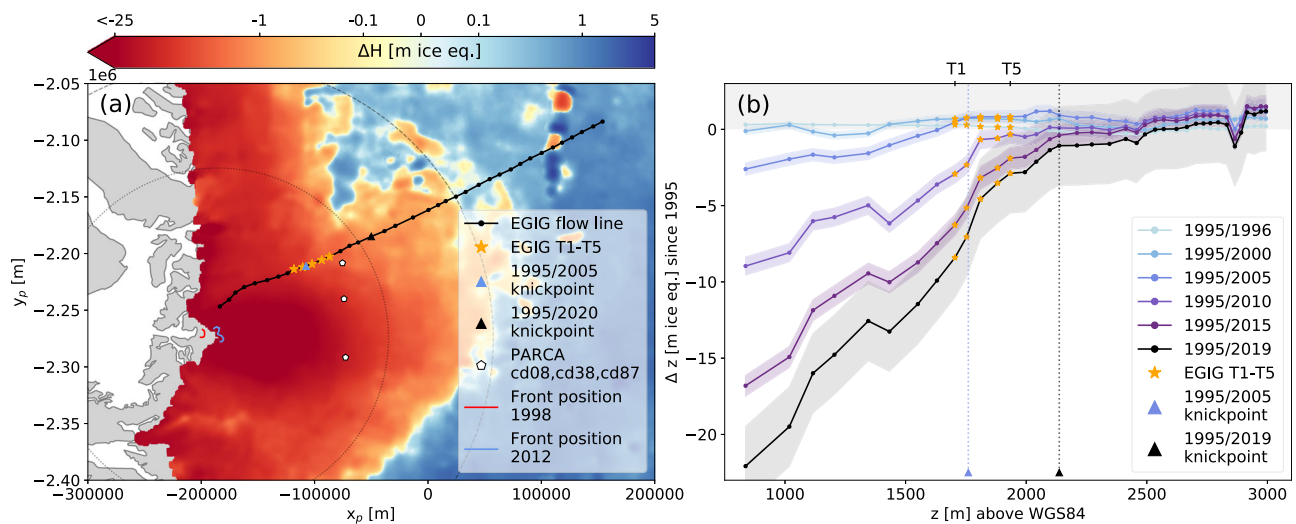


Fig. 4 | Knickpoint Migration. **a** Total cumulative surface elevation change from 1995–2020 altimetry data^{27,28}. Plotted on top is the flow-line cutting through the EGIG sites T1–T5, the location of PARCA sites cd08, cd38, cd87, estimated knickpoint locations for 2005 and 2019, Jakobshavn Isbræ front positions for 1998 and 2012, and two circles representing estimates of inland thinning limit^{32,89}. The depicted flow-line approximates the northern boundary of the catchment of Jakobshavn Isbræ. **b** Total surface elevation change along the flow-line through EGIG points (black) against surface elevation²⁹.

Digital Elevation Model (DEM), reflecting the 2018/2019 ice geometry²⁹, see Fig. 4b.

The surface elevation is insignificantly thickening at EGIG sites T1–T5 in the first 10-year period (1995–2005), after which, appreciable thinning is observed. The EGIG sites T1–T5 show considerable thinning of ~ 3–8 m in the 25-year period. The altimetry data shows a regional steepening of the surface slope over time, as the ice thins. We define the knickpoint as the point at which the ice surface switches from a relatively stable flat surface to a steeper gradient. With this definition, the knickpoint appears to have migrated far inland (> 100km) over the 15-year period after 2005, meaning that the cross-section of the ice sheet is becoming steeper in response to climate change³⁰.

The propagation of a dynamic thinning signal along a glacier has previously been modeled as a diffusive kinematic wave^{13,31–33}. We therefore view the position of the knickpoint as an indication of the arrival of a kinematic wave and estimate the wave speed. Felikson et al.³² utilized kinematic wave theory and analyzed Péclet numbers to predict an empirical inland upper bound, in which thinning from the front can propagate for individual catchments. At Jakobshavn Isbræ they determined the upper limit to be further inland than our observation sites. The kinematic wave has been shown to move very fast near the terminus of Jakobshavn Isbræ but is

assumed to slow down as it travels inland³³. The surface profiles seem to indicate the arrival of a kinematic wave at our observation sites for the first time around 2005 (Fig. 4b), although, we cannot be sure that this is a thinning signal that has traveled directly from the front of Jakobshavn Isbræ.

The knickpoint at our study site has moved ~ 82.2 km in the 14 years between 2005 and 2019, yielding a local kinematic wave speed of 5.9 km yr⁻¹. Considering a potential offset in the arrival time of the kinematic wave of ± 5 years yields high/low kinematic wave-speed estimates of 9.1 and 4.5 km yr⁻¹ respectively. The wave speed of seasonal signals, likely related to the increased availability of melt-water, has been observed in alpine glaciers, finding lower-end speeds of ~ 18–26 km yr⁻¹ and upper-end speeds of ~ 58–91 km yr⁻¹, which are considerably faster than our kinematic wave estimates³⁴. These alpine kinematic waves, however, are basal sliding anomalies propagating down-glacier. We suspect that the up-glacier kinematic wave we observed results from ice deformation as described below. This may also explain the discrepancy in wave propagation speed.

It is worth noting that, although some EGIG sites appear to be outside the catchment area of Jakobshavn Isbræ in Fig. 1, the glaciological community does not presently agree on the catchments precise shape and size. Several Greenland ice sheet catchment boundary products exist, using various methods and input data. For example, Zwally and Giovinetto³⁵,

Mouginot et al.³⁶, Mankoff et al.³⁷, and Krieger and Floricioiu³⁸. The catchment area of outlet glaciers of NEGIS has been found to vary up to 16% in area, using one method but various input data alone³⁹. The consistent change in both azimuth and velocities across the EGIG sites suggest that the sites are located inside the catchment of Jakobshavn Isbræ.

Discussion

Increasing velocity

The surface velocity of the ice sheet results from three components: internal deformation of the ice, sliding of the ice over the bed, and deformation of the bed itself⁴⁰. Various possible drivers, relating to either water or stresses, could cause an increase in one or more of these three components, resulting in an increased surface velocity.

Changes in basal sliding and sediment deformation due to changes in basal melt-water availability are unlikely to occur directly beneath our study sites. The surveyed sites are located more than 100 km from the front of Jakobshavn Isbræ, north of the main ice stream. This area is in the low accumulation, percolation zone⁴¹, and above the melt-water runoff limit, here approximated by the slush limit⁴². The slush limit is the uppermost visible summer appearance of water-saturated snow⁴³. As can be seen from Fig. 1, there was approximately ~10 km between T1 and the 2019 maximum slush limit and ~40 km to the 2021 maximum slush limit. We interpret the continued absence of an active supraglacial hydrology system to suggest there has been no recent change in basal hydrology associated with basal sliding and sediment deformation. These processes, however, could be happening at steady rates at our sites. The cumulative number of Positive Degree Days (PDD) for 2021–2023 were evaluated for the closest Greenland Climate Network (GC-NET) Automatic Weather station, Crawford Point^{44,45}. Crawford Point is located midway between EGIG sites T6 and T7. The final number of cumulative PDD was between 12 and 14 days. By comparison, 40–120 PDD were required per melt season to initiate seasonal enhancements in basal sliding at Swiss Camp in the late 1990s⁴⁶. See Supplement Fig. S9.

Seasonality in the observed velocities was also assessed. Normalized daily velocity estimates for all 11 sites were divided into summer days and non-summer days. Differences in the mean of the two groups were examined using an unpaired two-tailed t-test with 1% significance, for four different summer periods, see Supplement Fig. S10. In all four cases the null hypothesis, that the means of the two populations are the same, cannot be rejected. There is no statistical difference between the mean of the two groups. We, therefore, conclude that no seasonal signal was detected at the observation sites between 2020 and 2022. Supplement Fig. S10 shows the specific statistical values for each of the four tested cases.

Assuming our observed changes in ice-sheet velocity have occurred since c. 2005 when the knickpoint of the kinematic wave arrived in our study region, they are equivalent to ice-flow accelerations of ~3.9–10% per decade. Doyle et al.⁴⁷ (subsequently referred to as DS14) attributed in situ measurements of a similar inland ice-sheet acceleration equivalent to ~7% per decade, at site S10 in Southwest Greenland, to changes in basal sliding, not directly at S10 but further downstream, transmitted upstream to S10 through longitudinal stress-gradient coupling. Their attribution, however, was supported by a distinct seasonal velocity cycle, with summer velocities up to ~8% greater than winter velocities. They also find that an increase in mean winter velocity cannot be attributed to enhanced summer melt, suggesting a “longer-term change in sub-glacial hydrothermal regime”⁴⁷. While both S10 and our sites share some general similarities, being located between 50–70 km inland from the equilibrium line and between 1800–2000 m elevation in West Greenland, the absence of a distinct seasonal velocity cycle and supraglacial hydrology system at our sites does not provide the same justification for attributing our observed acceleration to basal sliding.

To further support this point, we evaluate whether longitudinal coupling stresses from enhanced sliding could have a large enough effect to explain our observed ice flow accelerations. The depth-averaged longitudinal coupling stresses were calculated along a flow-line close to T4, following the formulation presented in Van der Veen^{48,49}. The total driving

stress is the sum of the gravitational driving stress determined by the ice geometry, which in this case is assumed ‘fixed’, and the longitudinal coupling stress, dependent on along-flow gradients in basal sliding and ice thickness. It was found that under the assumption of no sliding, the longitudinal coupling stress has a magnitude of only 6% of the gravitational driving stress. A basal sliding perturbation of ~10 m yr⁻¹ introduced 1 km downstream of T4 was necessary to produce a 10% increase in the total driving stress through coupling stresses alone, see Supplement Fig. S11. This means it would require an along-flow strain rate of 0.01 yr⁻¹ to produce the observed acceleration at T4. This, however, is much larger than the observed change in strain rate between T3 and T4 of $\Delta\dot{\epsilon}_{xx} = 8.2 \cdot 10^{-5} \text{ yr}^{-1}$. Therefore, we believe longitudinal coupling from enhanced sliding alone cannot be responsible for the observed acceleration.

Williams et al.² (subsequently referred to as WS21) also did not detect any seasonality in the velocities of PARCA sites near Jakobshavn Isbræ. Their study compared NASA’s ITS-LIVE satellite-derived velocities with GPS observations from selected PARCA sites. This includes site cd38, also resurveyed in this study, and the additional site cd87, which are located in the main fast-flowing region, see Fig. 4. They found an acceleration at these two sites corresponding to a decadal rate of change of ~4.3% and 9.6%, respectively. Reanalyzing the WS21 data, we find double the increase in velocity at cd38, i.e., a decadal rate of change of 8.54%. WS21 attributes this acceleration to increased internal deformational velocity, as they find sufficient change in local ice geometry to produce a change in driving stress large enough to account for the observed speedup.

Similar to WS21, we explore the theoretical effect of changes in glacier geometry on driving stress and ice deformation⁵⁰. Using the simplifying assumption that ice deforms purely from simple shear, the surface velocity u_s can be expressed as the sum of the basal motion u_b and the velocity due to the shear deformation:

$$u_s = u_b + \frac{2A}{n+1} (\rho g H \sin S)^n H \quad (1)$$

Here, ρ is the ice density, H is the thickness of the ice column, S is the surface slope, n is the creep exponent, A the rate factor, and g is the gravitational acceleration. Using the common assumption of $n = 3$, the surface velocity is proportional to H^4 and $(\sin S)^3$. We create a sensitivity plot by assuming a relative change of $\pm 3\%$ in the ice thickness, δH , and $\pm 9\%$ in the surface slope δS , and no basal motion $u_b = 0$, see Fig. 5a–j. Generally, increasing the ice thickness will cause the ice to speed up, and so will the steepening of the ice surface slope.

We use the altimetry data to infer the ice thickness at the observation sites in 1995, by subtracting the total cumulative change in surface elevation from the 2018/2019 DEM. This allows us to assess changes in ice thickness δH and surface slope δS , and compare observed and expected velocity changes. The surface slope was calculated over three different length scales in order to estimate an upper and a lower bound on the contribution of changing geometry. The shortest length scale of ± 2 ice thicknesses (2H) corresponds to a distance of ~7 km, and the longest length scale of ± 15 ice thicknesses (15H) corresponds to ~54 km, see Supplementary Fig. S12. Assuming no changes in surface processes, such as mass balance and firn stratigraphy, the ice thickness was found to have thinned 2.6–8.2 m from 1995–2020 across the observation sites, corresponding to a 0.1–0.4% change in the ice column height.

The shorter the length scale over which surface slopes are calculated the more local variability the slope reflects, see Fig. 5a–j. The longest length scale, 15H, showed consistent steepening of the surface slope across all sites. The 5H length scale showed either steepening or close to no change in the surface slope, across all sites but T127. The 2H length scale showed much more variability, with the two sites T127 and T127a showing noticeable flattening of the surface while the remaining sites more closely follow the 5H and 15H surface slope changes. With the exception of site T2 and cd38, all sites show an insufficient increase in surface slope to overcome the decrease in thickness, for all three length scales. This means changes in local driving stress

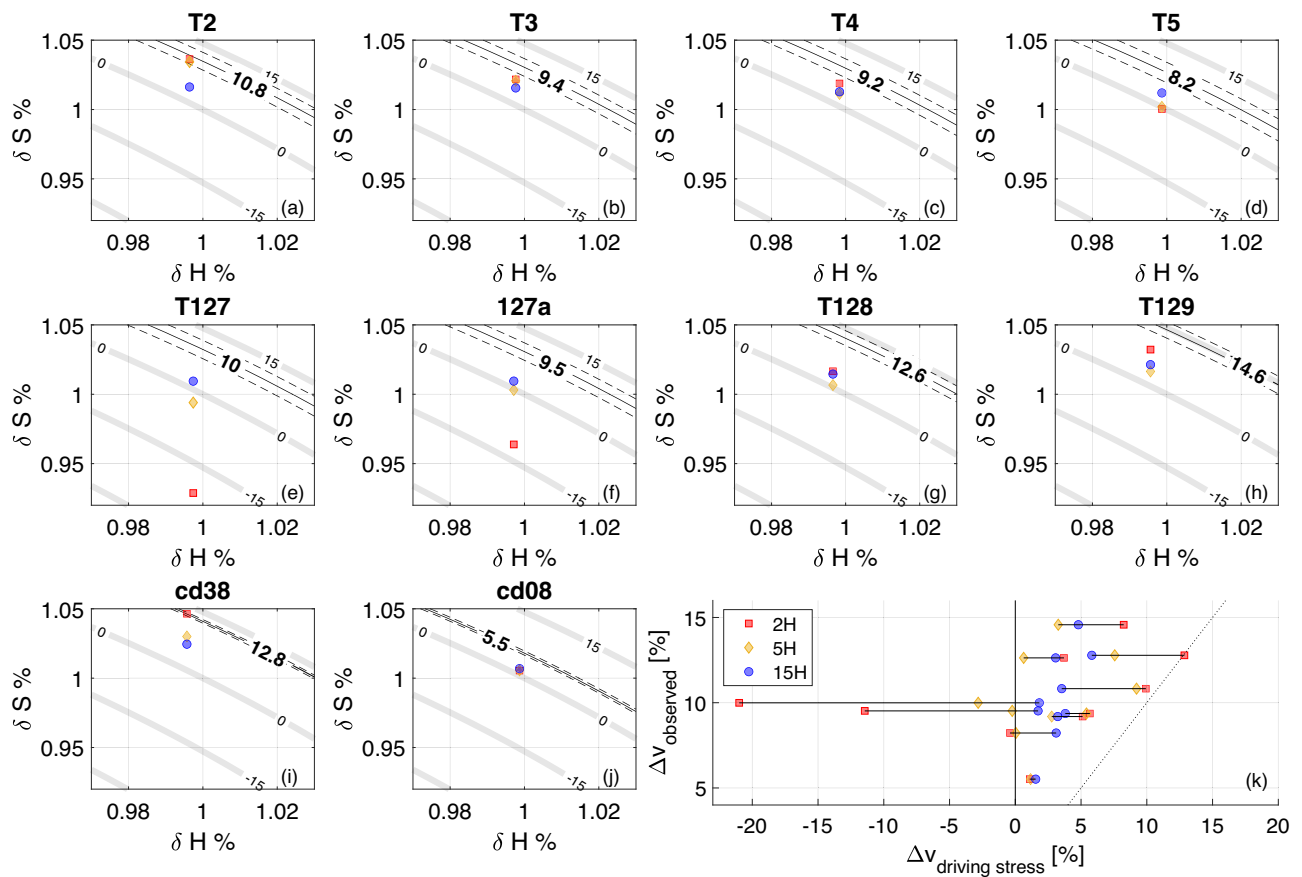


Fig. 5 | Effect of change in ice geometry on surface velocity. a–j Theoretical sensitivity plot for 10 of the observation sites. Each light gray contour shows the expected percentage change in surface velocity resulting from the combined change in ice thickness (δH) within the range of $\pm 3\%$ and surface slope δS in range $\pm 9\%$. The black solid line indicates the observed percentage increase in surface velocity, with uncertainties shown as black stippled lines. Also shown is the site-specific altimetry-derived change in ice thickness, estimated by updating the 2018/2019 DEM²⁰ by the 1995–2020 altimetry rate of change of surface elevation^{27,28}, and the

corresponding change in surface slope, calculated over three different length scales, indicated by the red, yellow and blue markers. The markers are labeled as, e.g., 2H referring to a range of ± 2 ice thickness, i.e., 4 ice thicknesses in total. k Calculated percentage change in surface velocity from the change in driving stress for each length scale plotted against the observed percentage change in velocity. The three cases of surface velocity change for each specific site are connected through a black line.

alone, associated with changes in ice geometry, cannot fully explain the acceleration we observe. Figure 5k shows a scatter plot of the observed and theoretical velocity changes. Here, the majority of the points lie well above the $x = y$ line for most of the points. Looking at points cd38 and T2 specifically in Fig. 5k we see that the calculated surface slope is subjected to more local variability in the ice geometry over the shortest length scale.

In contrast to WS21, we find ice geometry changes insufficient to explain the observed ice flow acceleration. This discrepancy could arise from, the difference in present-day geometry data used between the studies, the difference in cumulative surface elevation change data, or the chosen length scale to calculate the surface slope over. Both studies have examined site cd38, we find double the increase in velocity compared to WS21. This further points to the importance of in situ measurements when compared with historic observations.

Although longitudinal stress gradients are known to modify deformational ice flow, the longitudinal coupling length for ice sheets is theoretically 4–10 ice thickness⁵¹. With an ice thickness of ~ 1800 m in the middle of our study region, this corresponds to a coupling length of 7–18 km. This distance is much smaller than the region over which velocities are observed to increase. Longitudinal coupling is therefore assumed to be insufficient in importing an external velocity perturbation into our study region.

It is generally agreed that the disintegration of the floating tongue, initiated in 1997, caused an initial speed-up of Jakobshavn Isbræ^{14,17,52}. However, studies have shown that it is unlikely that the full speed-up can be

attributed to the immediate change in force balance resulting from the loss of the floating ice tongue. Additional mechanisms are required to further sustain and propagate the enhanced velocity and thinning inland^{18,19,53}. Possible candidates have been put forward including weakening of the shear margins^{18,22}, loss of buttressing, inland steepening of slopes, and thinning-induced changes in the effective pressure^{2,13,19,53,54}. Despite these efforts, the mechanism(s) remain a point of contention. We introduce creep instability as another possible mechanism below.

Shifting azimuth

The increase in azimuths means that there has been a northward deflection of the ice flow since the historical measurements. The PARCA study did not describe their method for calculating their reported azimuth values. Different methods of calculating azimuth values, for example, spherical or cartesian approaches, could result in an offset in values. Unlike the EGIG sites, we cannot check the azimuths of the PARCA sites by recalculation following equation (2), due to lack of information. Additionally, the PARCA measurements may differ from the EGIG measurements as they were made at a time when Jakobshavn Isbræ has been shown to be thickening and slowing down^{16,55}.

A potential influence on the observed change in azimuths is the appearance of crevasses in the time between surveys. We now observe large transverse crevasses, ~ 25 m wide, both open and snow-bridged, in various crevasse fields within our study area (Fig. 6). The presence of these crevasse

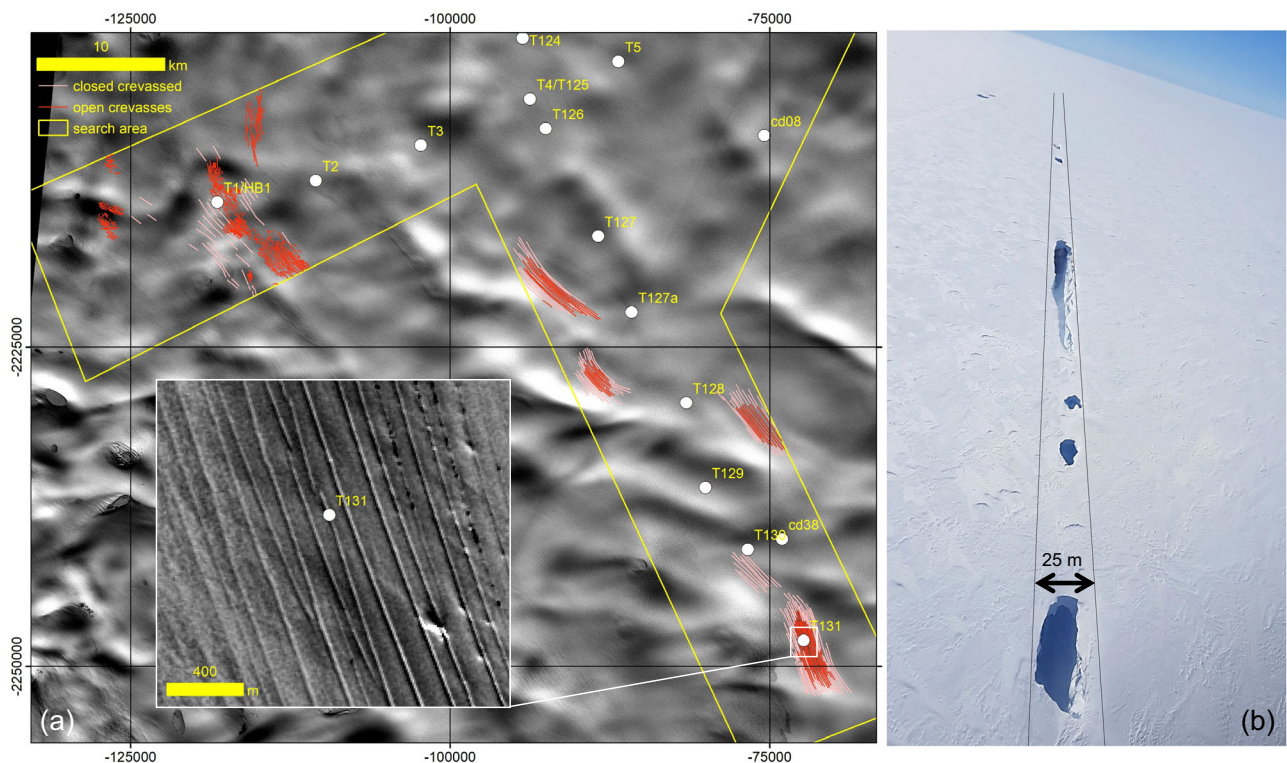


Fig. 6 | New crevasses disrupting continuous fluid mechanics. **a** Sentinel-2 visible image (band 4) acquired on 13 September 2018. Open and closed crevasses have been delineated within our study region. The inset shows a mix of open and closed

crevasses at T131 at the native pixel resolution of 10 by 10 m. **b** Oblique aerial photo acquired 15 June 2022 showing a partially snow-bridged linear transverse crevasse approximately 25 m wide in the vicinity of T128.

fields is relevant when interpreting ice-flow azimuth measurements, as the surface stress fields in the vicinity of large crevasses can deviate substantially from regional averages. This local reorganization of the surface stress field around crevasses, which is associated with a transition from fluid mechanics to fracture mechanics, is known to be linked to the mode of crevasse opening, but otherwise poorly understood in terms of magnitude or spatial extent⁵⁶. If the length scale over which crevasse fracture mechanics influence ice-flow azimuth is assumed to be limited to one ice thickness, then crevasse fracture processes should not influence ice-flow azimuth at all our measurement sites^{56,57}.

The crevasses that bisect the EGIG overland route in the vicinity of T131 must have formed sometime after the final 1967 EGIG traverse along that route. We speculate that the opening of this crevasse field is possibly associated with the arrival of the kinematic wave knickpoint in our study area. The recent appearance of major crevasses, however, qualitatively suggests that a fundamental shift in ice dynamics may now be underway in our study area. This also highlights a sharp contrast between the ice dynamic setting of our study area and the S10 site of DS14. While our study area is located inland from a fast tidewater glacier capable of initiating kinematic waves, S10 is located inland from a land-terminating ice margin. Consequently, the ice velocities at S10 are ~2–3 times less than our sites. Although DS14 suggests no nearby crevasses or moulins were present at S10 to allow surface melt to locally access the bed, crevasses have since been reported in the region of S10⁵⁸.

It is possible that the crevasses were present, but snow-covered, at the time of the EGIG expeditions and have since been uncovered. If that is the case, it might point to changing material properties of the snow and firn cover, due to the higher amount of re-frozen ice lenses, for example^{59,60}. If the firn has become thinner and more brittle in recent decades, it may no longer bridge such large crevasses.

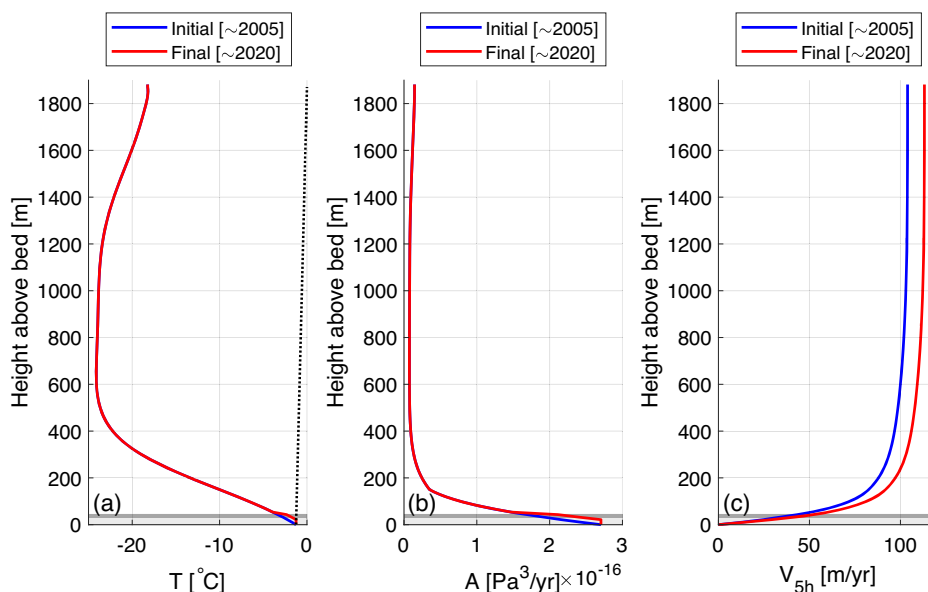
Observed surface flow azimuth generally reflects a combination of the basal sliding direction, governed by the local bedrock topography and the sub-glacial hydrological system, and the direction of flow from

internal deformation, governed by the regional surface slope of the ice. Zwally et al.⁴⁶ noticed a distinct temporary change in ice flow azimuth during the maximum seasonal acceleration of the ice at Swiss Camp, and speculated that it could be indicative of a change in basal friction, and by extension a change in the ratio between basal sliding and internal deformation. The in situ alpine glacier study by Engelhardt et al.⁶¹, reported deviations between surface flow direction and basal sliding direction of up to 30°. At lower elevations with Jakobshavn's ablation zone, despite substantial basal sliding, vertical variations in ice-flow azimuth have still been observed. There, in boreholes upstream of Issunguata Sermia, the upper portion of the ice column generally deforms along the surface slope, while the lowest portion of the ice column deforms along the bedrock slope⁶². Gundestrup and Hansen⁶³ studied the variation in azimuth with depth in a borehole drilled at DYE-3. They found azimuth fluctuating $\pm 15^\circ$ around an average value throughout most of the column, with jumps in the average azimuth value relating to changes in ice properties and the softness of the ice closer to the bed. Despite this difference in ice properties, the near-bed and surface azimuths aligned, as the majority of ice deformation occurs near the bed. In the context of our current study, this means that changes in near-bed deformation could potentially manifest as changes in the surface azimuth.

Creep instability

Consolidating this information, we propose that a limited form of creep instability is affecting basal conditions at inland sites, far away from the terminus region, acting to enhance the velocity and shift the azimuth at our surveyed sites⁶⁴. The creep instability is assumed to be restricted to the lower 15–20% of the ice column, where the majority of ice deformation occurs. This mechanism was originally presented by Clarke et al.⁶⁴ as a possible runaway increase of internal temperature and deformation rate of the ice, eventually leading to the formation of a temperate layer. We do not believe that such a temperate layer could develop from the diffusion of geothermal

Fig. 7 | Near-bed effective ice viscosity experiment for site T4. **a** PISM simulated temperature profile at site T4, with the dotted line indicating the pressure melting point temperature. **b** Corresponding value of the flow law parameter, A . **c** Corresponding theoretical vertical velocity profile. For all subplots, the blue curves show the initial pre-warming state, while red curves show changes after the height of the initial basal temperate layer (light gray band, 26 m) has been raised ~ 18 m (dark gray band, 43 m).



heat or changes to vertical velocity associated with changes in the surface mass balance. Rather it is assumed that the temperate layer would grow from a locally sourced mechanism, such as enhanced deformational heating or basal friction. Perhaps, dynamic thinning at the front can potentially instigate creep instability further inland, because of the dependence between effective ice viscosity, temperature, and deformational velocity. Small increases in deformation rate warm basal ice through strain heating, which in turn makes the basal ice softer and flow faster under the same driving stress and cause more strain heating⁶⁵.

To support this theory a simple case study is presented here, examining the required change in temperate layer height at site T4 needed to produce a 10% increase in the surface velocity. At present, no observed ice temperature profile exists at our observation sites⁶⁶. Borehole temperature observations from other areas of Jakobshavn Isbræ with differing ice-flow regimes show a thin temperate layer in the marginal slow-flowing regions⁶⁷, a 31 m thick temperate basal layer at drill site D approximately 50 km upstream from the calving front and adjacent to the fast channelized flow⁶⁸, and a thick temperate layer of ice, several hundreds of meters thick have been extrapolated at the center of the fast-flowing ice stream⁶⁹. However, the height of the center-line temperate layer has since come into question^{70–72}. A synthesis of simulated basal thermal state suggests that a large part of the catchment of Jakobshavn Isbræ is temperate, this includes beneath our study sites⁷³.

A best estimate temperature profile was extracted for site T4 from a thermomechanical ice-sheet simulation of Aschwanden et al.^{74,75}, Fig. 7a. The velocity profiles were calculated under the same assumptions as equation (1). When calculating the velocity profiles the ice was softened by an enhancement factor of $E = 2.5$ ⁷⁶ such that the surface velocity of the theoretical profile matched the observed surface velocity at T4 from 1959/1967 of 103 m yr⁻¹. The initial temperature profile showed a temperate basal layer of 26 m, corresponding to 1.4% of the 1882 m ice thickness. Although this initial temperate layer height seems reasonable considering the observed temperate layer thicknesses, the layer is likely too thin as using the relatively smooth BedMachine topography map in thermomechanical ice flow simulations produces a significantly thinner temperate ice layer, without sharp spatial gradients, than simulations using higher-roughness geostatistically simulated bed topography⁷⁷. This further suggests that the example we here depict for one site might not be characteristic of all the surveyed EGIG sites, because there can be sharp spatial gradients in temperate layer thickness. To explore the sensitivity between near-bed effective ice viscosity and surface velocities, the height of the basal temperate layer was changed manually. Raising the height of the basal temperate layer just ~ 18 m, was

enough to see an increase in surface velocity of $\sim 9.2\%$ from 103.9 m yr⁻¹ to 113.2 m yr⁻¹, similar in magnitude to the observed change at T4. This simple case study shows the potential effect of a relatively small increase in the basal temperate layer from 1.4% to 2.3% of the ice column, on the surface velocity.

Ultimately, creep instability could cause the inland migration, in both extent and thickness, of the temperate layer observed in Jakobshavn Isbræ's catchment⁶⁹. Clarke et al. suggest that ice at the boundary between frozen and thawed beds, where large longitudinal stresses are present, may be more susceptible to creep instability than uniformly thawed or frozen bedded ice. They expect that large longitudinal stresses are present in this boundary region, and speculate that the stress level in the confining cold ice will increase as more basal ice reaches the melting point. This may cause the basal temperature to increase to the melting point, the boundary region consequently migrating. Therefore, we speculate that the observed ice flow acceleration could be a physical manifestation that the temperate layer is now expanding in area throughout the Jakobshavn Isbræ catchment in response to a positive creep instability feedback between ice temperature, effective ice viscosity, and deformation. Perhaps counter intuitively, creep instability activates during times of ice sheet decay, drawdown, and thinning⁷⁸. It potentially triggers a change in effective ice viscosity in the lower layer of the ice column from the rapid drawdown and acceleration, which in turn can influence surface azimuths. A softening of the near-bed layer can change the vertical strain profile of the ice column, which can potentially influence the azimuth when ice flow is not isoazimuthal with depth⁶². Near-bed changes in the azimuth can also result from the transient redistribution of driving stress from basal slippery to basal sticky areas, associated with changes in the extent and thickness of the temperate layer⁷⁶. The appearance of major crevasses in the study region supports the conjecture that a fundamental shift in ice dynamics may be underway.

Conclusion

By comparing historic and newly acquired in situ velocity observations, we find accelerating ice flow > 100 km inland from the terminus, in the catchment of Jakobshavn Isbræ, outside the main fast-flowing channel. Although our observations cover a period of 60 years, these changes likely began less than 25 years ago at the terminus, and have since propagated up-glacier.

Previous studies^{2,47} also found surface velocity increases of comparable size at similar inland sites. DS14 found an increase of 7% per decade at S10, WS21 found 4.3–9.6% per decade at Jakobshavn, and this study found 3.9–10% per decade north of Jakobshavn Isbræ. However, we all attribute this increase to different mechanisms. DS14 finds clear indications of

changes in the sub-glacial hydrological system, postulating enhanced basal sliding, from increased surface melt further downstream transmitted upstream through longitudinal coupling stresses. This mechanism does not appear to be a driving force at our observation sites. WS21 finds that local geometric changes can explain the increase in surface velocity. We find, however, that changes in ice geometry are insufficient to explain the increase in surface velocity. We instead suggest a limited form of creep instability as an additional mechanism potentially aiding the inland propagation of enhanced ice flow. Softened near-bed effective ice viscosity can potentially explain coincident acceleration and rotation at our study sites. No studies have previously documented inland rotations.

As the east-west EGIG transect closely approximates the northern boundary of the Jakobshavn Isbræ ice-sheet catchment, a consistently shifting ice-flow direction there may have implications for the Jakobshavn Isbræ catchment area. Specifically, it appears that Jakobshavn Isbræ's catchment area may now be changing, deep inland, in response to the recent collapse of its floating tongue. From altimetry data, we find a local kinematic wave-speed inland of EGIG sites T1–T5 in the range 4.3–9.1 km yr⁻¹, with the best estimate of 5.9 km yr⁻¹. In comparison to estimated kinematic wave speeds for alpine glaciers, this is very slow. This highlights that the kinematic wave, likely initiated ~ 25 years ago, continues to propagate inland today.

A deep inland ice acceleration has recently been observed in response to terminus perturbation at the North East Greenland Ice Stream²⁰. Our observations now demonstrate deep inland ice acceleration in response to terminus perturbation at Jakobshavn Isbræ. Unlike the North East Greenland Ice Stream, however, our current observations highlight a deep inland acceleration occurring well outside any form of channelized ice flow. This suggests that the deep ice-sheet interior may actually be more sensitive to changes in ice flow than previously recognized. Specifically, a dynamic perturbation of Jakobshavn's terminus, initiated c. 25 years ago, now appears to be influencing non-channelized ice-sheet flow c. 100 km inland from the terminus.

More broadly, this work highlights the value of in situ GPS observations in resolving trends in ice velocity that are not otherwise detectable in remotely sensed ice velocities. Because of the sparsity of GPS surface velocity observations, the PARCA observations from the 1990s have been used as proxies for current-day velocities in some types of studies^{4,79}. Our results show a considerable divergence in observed velocities at PARCA sites cd08 and cd38 between the time of the PARCA campaign and today. Continuing the use of the PARCA observations as proxies for current-day velocities will be consequential for high-elevation input-output mass budget studies, that use an inland flux gate across which ice discharge is assumed constant⁴. Similarly, gravity studies that explicitly assume a covariance matrix to separate high and low-elevation mass trends⁸⁰, should consider the potential influence of non-trivial trends in high-elevation ice flow.

Methods

Historical velocity and azimuth

Recalculating the azimuth value, α , resulting from the reported change in position of each stake, was done using spherical trigonometry following⁸¹:

$$\alpha = \arctan\left(\frac{\cos(\phi_{59}) \sin(\lambda_{67} - \lambda_{59})}{\cos(\phi_{67}) \sin(\phi_{59}) - \sin(\phi_{67}) \cos(\phi_{59}) \cos(\lambda_{67} - \lambda_{59})}\right) \quad (2)$$

Here, ϕ are the latitudes and λ the longitudes of each respective stake. Before recalculating the velocity values, the observed positions were converted from longitude and latitude to projected coordinates, using the polar stereographic projection EPSG:3413. Velocity values were then simply calculated from the change in the reported observed position over time:

$$v = \frac{\sqrt{(x_{67} - x_{59})^2 + (y_{67} - y_{59})^2}}{t_{67} - t_{59}} \quad (3)$$

Here x and y represent the projected coordinates, and t is the time; the subscripts indicate the given year.

The original EGIG survey did not report uncertainty estimates for calculated velocity and azimuth values. Therefore, a Monte-Carlo simulation was used to estimate uncertainties for the recalculated velocity and azimuth values. The observed positions were randomly perturbed 1e6 times, by a distance within an assumed uncertainty of ± 11 m from the original 1959 and 1967 coordinates drawn from a uniform probability distribution (cf. supplementary section S2, Figure S3). Although the theodolite method used during the early EGIG campaigns accumulates uncertainties from the margin to the center of the ice sheet, a constant positional uncertainty (of ± 11 m) is assumed in the study region. This half-range value was chosen based on previously reported positional uncertainties. While some contemporaneous ice-sheet expeditions reported surveyed theodolite positions to the nearest ± 0.1 ⁸², the EGIG solved theodolite positions to the nearest ± 0.01 ²⁵. This approximates a theoretical EGIG positional uncertainty of ± 1 m, even across the central flow divide. Here, we conservatively assume an effective positional uncertainty of ± 10 m for the more marginal EGIG positions in which we are interested. An additional ± 1 m was included assuming the ellipsoid transformation might cause some slight shift in positions. The uncertainty of each calculated velocity value, δv , is taken as half the difference between the upper and the lower limit of the 95% confidence interval:

$$\delta v = \left| \frac{CI_{upper}^{95\%} - CI_{lower}^{95\%}}{2} \right| \quad (4)$$

GPS stations

We perform an in situ to in situ comparison of velocities. Supplementary Fig. S13 highlights the difficulties in comparing satellite-derived velocities with historic in situ velocity measurements; the noise in the satellite data is larger than the potential change between historic and current-day velocity values. We therefore chose to re-measure velocities using GPS rather than satellite observations.

Receivers and antennas were mounted on an aluminum scaffold, two meters above the snow surface. These GPS stations combine commercially available Javad GPS antennae and receivers with a custom-built 2800 mA battery bank powered by a 20 W solar panel, built by the Geological Survey of Denmark and Greenland (GEUS). The station set-up is shown in Supplementary Fig. S4.

We process the GPS data using the GIPSY-OASIS software package with kinematic data processing methods as described by ref. 20 and ref. 83. We use orbit and clock products of the Jet Propulsion Laboratory (JPL). JPL final orbit products, including satellite orbits and clock parameters, and Earth orientation parameters, including antenna phase center offset correction. The atmospheric delay parameters are modeled using the Vienna Mapping Function 1 (VMF1) with VMF1 grid nominals⁸⁴. We use amplitudes and phases of the main ocean tidal loading terms, calculated using the Automatic Loading Provider (<http://holt.oso.chalmers.se/loading/>), which are applied to the FES2014b ocean tide model including correction for the center of mass motion of the Earth owing to the ocean tides. The coordinates are computed in the EPSG:3413 frame.

GPS velocity and azimuth

The observed easting and northing velocity components were determined for each site, as the gradient of the line of best fit of the position-time plot. Figures of the position-time plots, and a more detailed description of outlier removal, can be found in supplementary results. Supplementary table S1 shows the determined easting and northing velocity components. The full magnitude of the velocity at each site was then calculated from simple trigonometry based on the easting

and northing components. The uncertainty of the velocity components, v_{unc} , was calculated as the product of the fractional uncertainty and the velocity

$$v_{unc} = \frac{\sqrt{\sigma(r_{i,x})^2 + \sigma(r_{i,y})^2}}{d_{site}} \cdot v_{site} \quad (5)$$

Here, the first term is the fractional uncertainty, where the numerator is the positional uncertainty given by $\sigma(r_{i,x})$ and $\sigma(r_{i,y})$, the standard deviation of all the residuals for the x- and y-component respectively, and the denominator, d_{site} , is the total distance moved over the observation period for each respective stake. v_{site} is the derived velocity magnitude of each respective stake for the entire observation period.

The azimuths are again calculated following equation (2). The present-day GPS-derived azimuth uncertainty is set to $\pm 1^\circ$ for all sites. This value is based on how azimuth uncertainty was estimated in a similar GPS processing method during our contemporaneous study of much slower-flowing ice at Camp Century³. The mean positional uncertainty for all 11 sites is 0.0204 m, while the mean velocity uncertainty for all 11 sites is $\pm 0.2545 \text{ m yr}^{-1}$.

We also looked into the effect of tectonic plate movement on the observed velocities. Using the online tool Plate Motion Calculator (<https://www.unavco.org/software/geodetic-utilities/plate-motion-calculator/plate-motion-calculator.html>) and plate-motion model ITRF2014⁸⁵, the plate velocity components at each of the 11 observation sites, were found to have a magnitude ranging between 13–16 mm yr^{-1} . Since the plate velocity is four orders of magnitude smaller than the ice velocities, it was decided not to correct for this movement.

Data availability

Both processed and un-processed GPS data are available from the GEUS Dataverse <https://doi.org/10.22008/FK2/EP6P4O>.

Received: 5 April 2023; Accepted: 14 March 2024;
Published online: 24 April 2024

References

1. Tedstone, A. J. et al. Decadal slowdown of a land-terminating sector of the Greenland ice sheet despite warming. *Nature* **526**, 692–695 (2015).
2. Williams, J. J., Gourmelen, N. & Nienow, P. Complex multi-decadal ice dynamical change inland of marine-terminating glaciers on the Greenland ice sheet. *J. Glaciol.* **67**, 833–846 (2021).
3. Colgan, W. et al. Sixty years of ice form and flow at Camp Century, Greenland. *J. Glaciol.* **69**, 919–929 (2023).
4. Colgan, W. et al. Greenland high-elevation mass balance: inference and implication of reference period (1961–90) imbalance. *Ann. Glaciol.* **56**, 105–117 (2015).
5. Joughin, I. et al. Seasonal speedup along the western flank of the Greenland ice sheet. *Science* **320**, 781–783 (2008).
6. Sundal, A. V. et al. Melt-induced speed-up of Greenland ice sheet offset by efficient subglacial drainage. *Nature* **469**, 521–524 (2011).
7. Khan, S. A. et al. Greenland ice sheet mass balance: a review. *Rep. Prog. Phys.* **78**, 046801 (2015).
8. Mouginot, J. et al. Forty-six years of Greenland ice sheet mass balance from 1972 to 2018. *Proc. Natl Acad. Sci. USA* **116**, 9239–9244 (2019).
9. van den Broeke, M. et al. Partitioning recent Greenland mass loss. *Science* **326**, 984–986 (2009).
10. Hanna, E. et al. Increased runoff from melt from the Greenland ice sheet: a response to global warming. *J. Clim.* **21**, 331–341 (2008).
11. Aschwanden, A. et al. Contribution of the Greenland ice sheet to sea level over the next millennium. *Sci. Adv.* **5**, eaav9396 (2019).
12. King, M. D. et al. Dynamic ice loss from the Greenland ice sheet driven by sustained glacier retreat. *Commun. Earth Environ.* **1**, 1–7 (2020).
13. Pfeffer, W. T. A simple mechanism for irreversible tidewater glacier retreat. *J. Geophys. Res. Earth Surf.* **112**, 1–12 (2007).
14. Motyka, R. J. et al. Submarine melting of the 1985 Jakobshavn Isbræ floating tongue and the triggering of the current retreat. *J. Geophys. Res. Earth Surf.* **116**, F01007 (2011).
15. Thomas, R. H. Force-perturbation analysis of recent thinning and acceleration of Jakobshavn Isbræ, Greenland. *J. Glaciol.* **50**, 57–66 (2004).
16. Joughin, I., Abdalati, W. & Fahnestock, M. Large fluctuations in speed on Greenland’s Jakobshavn Isbræ glacier. *Nature* **432**, 608–610 (2004).
17. Joughin, I. et al. Continued evolution of Jakobshavn Isbræ following its rapid speedup. *J. Geophys. Res. Earth Surf.* **113**, F04006 (2008).
18. Van Der Veen, C. J., Plummer, J. & Stearns, L. A. Controls on the recent speed-up of Jakobshavn Isbræ, West Greenland. *J. Glaciol.* **57**, 770–782 (2011).
19. Vieli, A. & Nick, F. M. Understanding and modelling rapid dynamic changes of tidewater outlet glaciers: issues and implications. *Surv. Geophys.* **32**, 437–458 (2011).
20. Khan, S. A. et al. Extensive inland thinning and speed-up of northeast Greenland ice stream. *Nature* **611**, 727–732 (2022).
21. Moon, T. et al. Distinct patterns of seasonal Greenland glacier velocity. *Geophys. Res. Lett.* **41**, 7209–7216 (2014).
22. Bondzio, J. H. et al. The mechanisms behind Jakobshavn Isbræ’s acceleration and mass loss: A 3-D thermomechanical model study. *Geophys. Res. Lett.* **44**, 6252–6260 (2017).
23. Thomas, R. H., Csathó, B. M., Gogineni, S., Jezek, K. C. & Kuivinen, K. Thickening of the western part of the Greenland ice sheet. *J. Glaciol.* **44**, 653–658 (1998).
24. Homann, C., Möller, D., Salbach, H. & Stengele, R. Die weiterführung der geodätischen arbeiten der internationalen glaziologischen grönländ-expedition (egig) durch das institute für vermessungskunde der tu braunschweig 1987–1993. *Tech. Rep.* 303 (Verlag der Bayerischen Akademie der Wissenschaften, 1996).
25. Heimes, F.-J., Hofmann, W., Karsten, A., Nottarp, K. & Stober, M. Die deutschen geodätischen arbeiten im rahmen der internationalen glaziologischen grönländ-expedition (egig) 1959–1974. *Tech. Rep.* 281 (Verlag der Bayerischen Akademie der Wissenschaften, 1986).
26. Morlighem, M. et al. Bedmachine v3: Complete bed topography and ocean bathymetry mapping of Greenland from multibeam echo sounding combined with mass conservation. *Geophys. Res. Lett.* **44**, 11–051 (2017).
27. Khan, S. A. et al. Geodetic measurements reveal similarities between post-last glacial maximum and present-day mass loss from the Greenland ice sheet. *Sci. Adv.* **2**, e1600931 (2016).
28. Khan, S. A. et al. Greenland mass trends from airborne and satellite altimetry during 2011–2020. *J. Geophys. Res. Earth Surf.* **127**, e2021JF006505 (2022).
29. Fan, Y., Ke, C.-Q. & Shen, X. A new Greenland digital elevation model derived from icesat-2 during 2018–2019. *Earth Syst. Sci. Data* **14**, 781–794 (2022).
30. Parizek, B. R. & Alley, R. B. Implications of increased Greenland surface melt under global-warming scenarios: ice-sheet simulations. *Quater. Sci. Rev.* **23**, 1013–1027 (2004).
31. van der Veen, C. J. Greenland ice sheet response to external forcing. *J. Geophys. Res. Atmos.* **106**, 34047–34058 (2001).
32. Felikson, D. et al. Inland thinning on the Greenland ice sheet controlled by outlet glacier geometry. *Nat. Geosci.* **10**, 366–369 (2017).
33. Riel, B., Minchew, B. & Joughin, I. Observing traveling waves in glaciers with remote sensing: new flexible time series methods and application to Sermeq Kujalleq (Jakobshavn Isbræ), Greenland. *Cryosphere* **15**, 407–429 (2021).

34. Willis, I. C. Intra-annual variations in glacier motion: a review. *Prog. Phys. Geogr.* **19**, 61–106 (1995).
35. Zwally, H. J. & Giovinetto, M. B. Balance mass flux and ice velocity across the equilibrium line in drainage systems of Greenland. *J. Geophys. Res. Atmos.* **106**, 33717–33728 (2001).
36. Mouginot, J. & Rignot, E. Glacier catchments/basins for the Greenland ice sheet [data set], dryad. <https://datadryad.org/stash/dataset/doi:10.7280/D1WT11> (2019).
37. Mankoff, K. D. et al. Greenland liquid water discharge from 1958 through 2019. *Earth Syst. Sci. Data* **12**, 2811–2841 (2020).
38. Kriegera, L. & Floricioiu, D. Modified watershed processing with sar velocities for individual glacier drainage basins on ice sheets. In: *EUSAR 2021; 13th European Conference on Synthetic Aperture Radar*, 1–4 (VDE Verlag, 2021).
39. Krieger, L., Floricioiu, D. & Neckel, N. Drainage basin delineation for outlet glaciers of northeast Greenland based on sentinel-1 ice velocities and tandem-x elevations. *Remote Sens. Environ.* **237**, 111483 (2020).
40. Cuffey, K. M. & Paterson, W. S. B. *The Physics of Glaciers* (Academic Press, 2010).
41. Vandecrux, B. et al. Firn data compilation reveals widespread decrease of firn air content in western Greenland. *Cryosphere* **13**, 845–859 (2019).
42. Machguth, H., Tedstone, A. J. & Mattea, E. Code and data: slush limits of the western flank of the Greenland ice sheet, mapped from modis, 2000-2021 (version v1) [data set] <https://doi.org/10.5281/zenodo.6892165> (2022).
43. Machguth, H., Tedstone, A. J. & Mattea, E. Daily variations in Western Greenland slush limits, 2000–2021. *J. Glaciol.* **69**, 191–203 (2023).
44. Steffen, K. et al. GC-Net Level 1 historical automated weather station data. <https://doi.org/10.22008/FK2/VVXGUT> (2022).
45. How, P. et al. Cp1_day.csv <https://doi.org/10.22008/FK2/IW73UU/PTVGXV> (2022).
46. Zwally, H. J. et al. Surface melt-induced acceleration of Greenland ice-sheet flow. *Science* **297**, 218–222 (2002).
47. Doyle, S. H. et al. Persistent flow acceleration within the interior of the Greenland ice sheet. *Geophys. Res. Lett.* **41**, 899–905 (2014).
48. Van der Veen, C. Longitudinal stresses and basal sliding: a comparative study. In: Van der Veen, C. & Oerlemans, J. (eds.) *Dynamics of the West Antarctic ice sheet: Proceedings of a Workshop held in Utrecht, May 6–8, 1985*, 223–248. Springer Netherlands, Dordrecht: (Reidel Publishing Company, 1987).
49. Colgan, W., Pfeffer, W. T., Rajaram, H., Abdalati, W. & Balog, J. Monte carlo ice flow modeling projects a new stable configuration for columbia glacier, alaska, c. 2020. *Cryosphere* **6**, 1395–1409 (2012).
50. Nishimura, D., Sugiyama, S., Bauder, A. & Funk, M. Changes in ice-flow velocity and surface elevation from 1874 to 2006 in Rhonegletscher, Switzerland. *Arctic Antarctic Alpine Res.* **45**, 552–562 (2013).
51. Kamb, B. & Echelmeyer, K. A. Stress-gradient coupling in glacier flow: I. longitudinal averaging of the influence of ice thickness and surface slope. *J. Glaciol.* **32**, 267–284 (1986).
52. Nick, F. M., Vieli, A., Howat, I. M. & Joughin, I. Large-scale changes in Greenland outlet glacier dynamics triggered at the terminus. *Nat. Geosci.* **2**, 110–114 (2009).
53. Joughin, I. et al. Seasonal to decadal scale variations in the surface velocity of Jakobshavn Isbrae, Greenland: observation and model-based analysis. *J. Geophys. Res. Earth Surf.* **117**, F02030 (2012).
54. Howat, I. M., Smith, B. E., Joughin, I. & Scambos, T. A. Rates of southeast Greenland ice volume loss from combined icesat and aster observations. *Geophys. Res. Lett.* **35**, L17505 (2008).
55. Thomas, R. H. et al. Investigation of surface melting and dynamic thinning on Jakobshavn Isbræ, Greenland. *J. Glaciol.* **49**, 231–239 (2003).
56. Colgan, W. et al. Glacier crevasses: observations, models, and mass balance implications. *Rev. Geophys.* **54**, 119–161 (2016).
57. Meier, M. F. et al. *Preliminary study of crevasse formation: blue ice valley, Greenland, 1955*. Technical Report 38 (U.S. Army Snow, Ice, and Permafrost Research Establishment, 1957).
58. Christoffersen, P. et al. Cascading lake drainage on the Greenland ice sheet triggered by tensile shock and fracture. *Nat. Commun.* **9**, 1064 (2018).
59. Machguth, H. et al. Greenland meltwater storage in firn limited by near-surface ice formation. *Nat. Clim. Chang.* **6**, 390–393 (2016).
60. MacFerrin, M. et al. Rapid expansion of Greenland’s low-permeability ice slabs. *Nature* **573**, 403–407 (2019).
61. Engelhardt, H. F., Harrison, W. D. & Kamb, B. Basal sliding and conditions at the glacier bed as revealed by bore-hole photography. *J. Glaciol.* **20**, 469–508 (1978).
62. Thompson-Munson, M. E. *Observations and Implications of three-dimensional deformation in the Greenland Ice Sheet*. Master’s Thesis. (University of Wyoming, 2020).
63. Gundestrup, N. S. & Hansen, B. L. Bore-hole survey at dye 3, south Greenland. *J. Glaciol.* **30**, 282–288 (1984).
64. Clarke, G. K., Nitsan, U. & Paterson, W. Strain heating and creep instability in glaciers and ice sheets. *Rev. Geophys.* **15**, 235–247 (1977).
65. Colgan, W., Sommers, A., Rajaram, H., Abdalati, W. & Frahm, J. Considering thermal-viscous collapse of the greenland ice sheet. *Earth’s Future* **3**, 252–267 (2015).
66. Løkkegaard, A. et al. Greenland and Canadian Arctic ice temperature profiles database. *Cryosphere* **17**, 3829–3845 (2023).
67. Thomsen, H., Olesen, O. B., Braithwaite, R. J. & Bøggild, C. E. Ice drilling and mass balance at Pâkitsoq, Jakobshavn, Central West Greenland. *Rapport Grønlands Geologiske Undersøgelse* **152**, 80–84 (1991).
68. Lüthi, M., Funk, M., Iken, A., Gogineni, S. & Truffer, M. Mechanisms of fast flow in Jakobshavn Isbræ, West Greenland: Part III. measurements of ice deformation, temperature and cross-borehole conductivity in boreholes to the bedrock. *J. Glaciol.* **48**, 369–385 (2002).
69. Iken, A., Echelmeyer, K., Harrison, W. & Funk, M. Mechanisms of fast flow in Jakobshavn Isbrae, West Greenland: part I. Measurements of temperature and water level in deep boreholes. *J. Glaciol.* **39**, 15–25 (1993).
70. Suckale, J., Platt, J. D., Perol, T. & Rice, J. R. Deformation-induced melting in the margins of the west antarctic ice streams. *J. Geophys. Res. Earth Surf.* **119**, 1004–1025 (2014).
71. Shapero, D. R., Joughin, I. R., Poinar, K., Morthighem, M. & Gillet-Chaulet, F. Basal resistance for three of the largest Greenland outlet glaciers. *J. Geophys. Res. Earth Surf.* **121**, 168–180 (2016).
72. Doyle, S. H. et al. Physical conditions of fast glacier flow: 1. measurements from boreholes drilled to the bed of store glacier, West Greenland. *J. Geophys. Res. Earth Surf.* **123**, 324–348 (2018).
73. MacGregor, J. A. et al. Gbatsv2: a revised synthesis of the likely basal thermal state of the Greenland ice sheet. *Cryosphere* **16**, 3033–3049 (2022).
74. Aschwanden, A., Fahnestock, M. A. & Truffer, M. Complex Greenland outlet glacier flow captured. *Nat. Commun.* **7**, 1–8 (2016).
75. Bueler, E. & Brown, J. Shallow shelf approximation as a “sliding law” in a thermodynamically coupled ice sheet model. *J. Geophys. Res.* **114**, F03008 (2009).
76. Ryser, C. et al. Sustained high basal motion of the Greenland ice sheet revealed by borehole deformation. *J. Glaciol.* **60**, 647–660 (2014).
77. Law, R. et al. Complex motion of Greenland ice sheet outlet glaciers with basal temperate ice. *Sci. Adv.* **9**, eabq5180 (2023).
78. Payne, A. Limit cycles in the basal thermal regime of ice sheets. *J. Geophys. Res. Solid Earth* **100**, 4249–4263 (1995).

79. Colgan, W. et al. Greenland ice sheet mass balance assessed by promice (1995–2015). *Geol. Surv. Denmark Greenland (GEUS) Bull.* **43**, e2019430201 (2019).
80. Luthcke, S. B. et al. Recent Greenland ice mass loss by drainage system from satellite gravity observations. *Science* **314**, 1286–1289 (2006).
81. Snyder, J. P. *Map Projections—A Working Manual*, Vol. 1395 (US Government Printing Office, 1987).
82. Paterson, W. S. B. & Slessor, C. G. M. Trigonometric levelling across the inland ice in north Greenland. *Empire Surv. Rev.* **13**, 252–261 (1956).
83. Christmann, J. et al. Elastic deformation plays a non-negligible role in Greenland's outlet glacier flow. *Commun. Earth Environ.* **2**, 232 (2021).
84. Boehm, J., Werl, B. & Schuh, H. Troposphere mapping functions for GPS and very long baseline interferometry from European center for medium-range weather forecasts operational analysis data. *J. Geophys. Res. Solid Earth* **111**, B02406 (2006).
85. Altamimi, Z., Rebischung, P., Métivier, L. & Collilioux, X. Itrf2014: a new release of the international terrestrial reference frame modeling nonlinear station motions. *J. Geophys. Res. Solid Earth* **121**, 6109–6131 (2016).
86. Gardner, A. S., Fahnestock, M. & Scambos, T. A. *Its_live Regional Glacier and Ice Sheet Surface Velocities*. (National Snow and Ice Data Center, 2019).
87. MacGregor, J. A. et al. The age of surface-exposed ice along the northern margin of the greenland ice sheet. *J. Glaciol.* **66**, 667–684 (2020).
88. Moon, T., Fisher, M., Harden, L. & Stafford, T. Qgreenland (v1. 0.1). *software*. Available from <https://qgreenland.org>. <https://doi.org/10.5281/zenodo.4558266> (2021).
89. Felikson, D., A. Catania, G., Bartholomaeus, T. C., Morlighem, M. & Noël, B. P. Y. Steep glacier bed knickpoints mitigate inland thinning in Greenland. *Geophys. Res. Lett.* **48**, e2020GL090112 (2021).

Acknowledgements

The author team thanks Henrik Spanggård for his help with data collection and logistics and Baptiste Vandecrux for providing the snow zone delineations. Data from the Greenland Climate Network (GC-Net) Program are provided by the Geological Survey of Denmark and Greenland (GEUS) at <https://doi.org/10.22008/FK2/IW73UU/MSZG4S>. This work would not have been possible without the incredible work done by all the people associated with both the EGIG and PARCA campaigns. The author team would also like to thank Lauren C. Andrews, Samuel Doyle, and the anonymous reviewer whose comments pushed us to greatly improve this manuscript. This work was supported by the Independent Research Fund Denmark (IRFD) award number 8049-00003 ("Unraveling the response time-scales of Greenland's most critical glacier"). S.A.K. and W.C. acknowledge support from the

Carlsberg Foundation—Semper Ardens Advance program (grant no. CF22-0628).

Author contributions

A.L. conducted the formal analysis and visualization. W.C. and S.A.K. acquired the funding, designed the study, planned the fieldwork, and supervised the study. A.L., W.C., S.A.K., K.H., K.T. conducted the field measurements. S.A.K. and J.J. processed the GPS data. A.L., W.C., and S.A.K. discussed and interpreted the results and are in charge of the data curation. All authors contributed to the writing and editing process.

Competing interests

The authors declare no competing interests.

Additional information

Supplementary information The online version contains supplementary material available at <https://doi.org/10.1038/s43247-024-01322-w>.

Correspondence and requests for materials should be addressed to Anja Løkkegaard.

Peer review information *Communications Earth & Environment* thanks Samuel Doyle and the other, anonymous, reviewer(s) for their contribution to the peer review of this work. Primary handling editors: Shin Sugiyama, Heike Langenberg. A peer review file is available.

Reprints and permissions information is available at <http://www.nature.com/reprints>

Publisher's note Springer Nature remains neutral with regard to jurisdictional claims in published maps and institutional affiliations.

Open Access This article is licensed under a Creative Commons Attribution 4.0 International License, which permits use, sharing, adaptation, distribution and reproduction in any medium or format, as long as you give appropriate credit to the original author(s) and the source, provide a link to the Creative Commons licence, and indicate if changes were made. The images or other third party material in this article are included in the article's Creative Commons licence, unless indicated otherwise in a credit line to the material. If material is not included in the article's Creative Commons licence and your intended use is not permitted by statutory regulation or exceeds the permitted use, you will need to obtain permission directly from the copyright holder. To view a copy of this licence, visit <http://creativecommons.org/licenses/by/4.0/>.

© The Author(s) 2024